Reflection-asymmetric wormholes and their double shadows

Maciek Wielgus*
Black Hole Initiative at Harvard University, 20 Garden Street, Cambridge, Massachusetts 02138, USA and Center for Astrophysics, Harvard & Smithsonian, 60 Garden Street, Cambridge, Massachusetts 02138, USA

Jiří Horák
Astronomical Institute, Academy of Sciences, Bočni II 1401, CZ-14131 Prague, Czech Republic

Frederic Vincent
LESIA, Observatoire de Paris, Université PSL, CNRS, Sorbonne Universités, UPMC Univ. Paris 06, Univ. de Paris, Sorbonne Paris Cité, 5 place Jules Janssen, 92195 Meudon, France

Marek Abramowicz
Nicolaus Copernicus Astronomical Centre, Polish Academy of Sciences, Bartycka 18, 00-716 Warsaw, Poland; Research Center for Computational Physics and Data Processing; Institute of Physics, Silesian University in Opava, Bezručovo náměstí, 1150/13,746 01 Opava, Czech Republic and Department of Physics, Göteborg University, 412-96 Göteborg, Sweden

(Received 23 August 2020; accepted 9 September 2020; published 20 October 2020)

We discuss construction and observational properties of wormholes obtained by connecting two Reissner-Nordström spacetimes with distinct mass and charge parameters. These objects are spherically symmetric, but not reflection symmetric, as the connected spacetimes differ. The reflection-asymmetric wormholes may reflect a significant fraction of the infalling radiation back to the spacetime of its origin. We interpret this effect in a simple framework of the effective photon potential. Depending on the model parameters, image of such a wormhole seen by a distant observer (its "shadow") may contain a photon ring formed on the observer's side, photon ring formed on the other side of the wormhole, or both photon rings. These unique topological features would allow us to firmly distinguish this class of objects from Kerr black holes using radioastronomical observations.

DOI: 10.1103/PhysRevD.102.084044

I. INTRODUCTION

Traversable wormholes are spacetime tunnels connecting universes or distant parts of the same universe, through which transit of mass and energy is possible. They were proposed and discussed by Ellis [1] and later by Morris *et al.* [2]. A particularly simple construction, a symmetric wormhole obtained by surgically grafting two Schwarzschild spacetimes (cut-and-paste procedure), was given by Visser [3]. A thin spherical layer of exotic matter (violating the weak energy condition of non-negative energy density), concentrated at the junction between the two connected spacetimes, is required to fulfill the Einstein field equations and to stabilize the wormhole. Similar requirements are common to a broader class of wormholes consistent with the general relativity [4]. Alternative theories of gravity [5–7], or general relativity in higher number of dimensions [8], may admit wormhole solutions without invoking the exotic stress-energy tensor.

In recent years, a lot of research has been dedicated to calculating the appearance of wormholes illuminated by the electromagnetic radiation [9–17]. This interest has been sparkled, at least in part, by the developments in the radio-interferometry and assemblement of the Event Horizon Telescope (EHT). The EHT is able to resolve the event horizon scale structure for at least two nearby objects, our Galactic Center [18], and the center of the M87 galaxy [19–21], with a potential to resolve many more sources in the future [22,23]. At this point, it becomes possible to observationally distinguish between black holes and certain classes of black hole mimickers [24,25]. Wormholes constitute an important type of the latter, as an example of horizonless spacetimes that may be identical to the black hole spacetime everywhere apart from its most internal part.

Spacetimes of compact objects may admit unstable spherical null geodesics [26,27], forming a photon sphere. The null geodesics approaching these unstable spherical orbits arbitrarily close create a critical curve on a distant observer's screen [28,29]. The size and shape of that curve are dictated

*maciek.wielgus@gmail.com

entirely by the geometry of spacetime and not by the geometry of the source of the radiation. In case of Kerr black holes, critical curves surrounding a dark "shadow" region were first rigorously studied by Bardeen [30] and Luminet [31]. While this asymptotic feature itself is not observable, in a realistic astrophysical scenario, we expect an image of a compact object to contain sharp features approximating the critical curves—"photon rings," corresponding to photon trajectories approaching the spherical geodesics [25,28,29,32]. The amount of flux transported along these geodesics is enhanced, as a consequence of an increased path through the radiation-emitting region surrounding the compact object. Photon rings could be, at least in principle, identified with very high angular resolution radiointerferometric observations [29,32]. In this paper, we study the critical curves, but we occasionally refer to the results as photon rings or shadows, which are somewhat imprecise, but follow a common convention in the literature. We avoid using the "Einstein ring" term, commonly associated with a scenario requiring a very specific geometric arrangement of the system and involving much smaller deflection angles [33].

We discuss critical curves for a class of wormholes distinguished by the asymmetry between the spacetimes they connect, a "reflection" asymmetry with respect to the wormhole throat [34–36]. As a representative model example, we discuss in more detail wormholes connecting two Reissner-Nordström spacetimes, following the reflection-symmetric constructions considered by [3,37,38]. However, in our case, Reissner-Nordström spacetimes on both sides of the wormhole are characterized by generally different masses $M_{1,2}$ and charge parameters $\mathcal{Q}_{1,2}$. Because of the spherical symmetry of the spacetimes that we consider, the shadows remain circularly symmetric. Nevertheless, the reflection asymmetry of the wormhole spacetime has significant consequences for the associated shadow, which may indicate the presence of a secondary component, corresponding to the unstable photon sphere from the other side of the wormhole, or even consist exclusively of the component from the other side, that may not match the gravitational signature of the spacetime on the side of the observer. Hence, we define a class of black hole mimickers that may indicate observational features topologically distinct from that of Kerr black holes and could potentially be distinguished with the future observations.

II. EFFECTIVE PHOTON POTENTIAL OF A WORMHOLE

Let us consider a spherically symmetric spacetime with metric $g_{\mu\nu}$ in spherical coordinates $\{t, r, \theta, \phi\}$,

$$\mathrm{d}s^2 = g_{\mu\nu}\mathrm{d}x^\mu \mathrm{d}x^\nu = -f\mathrm{d}t^2 + f^{-1}\mathrm{d}r^2 + r^2(\mathrm{d}\theta^2 + \sin^2\theta \mathrm{d}\phi^2), \tag{1}$$

where the function $f \equiv f(r)$ will be specified later and we employ the $(-+++)$ signature. For an equatorial null geodesic, it follows from the condition $p^\mu p_\mu = 0$ that

$$\frac{p_t^2}{f} - \frac{p_\phi^2}{r^2} = \frac{(p^r)^2}{f}, \tag{2}$$

where $p^\mu = \mathrm{d}x^\mu/\mathrm{d}s$ is a photon four-momentum and s is a properly chosen affine parameter. The components p_t and p_ϕ are conserved along the geodesic due to the Killing symmetries of the considered spacetime. Their ratio $b = -p_\phi/p_t$ is the impact parameter of the photon (also referred to as a specific angular momentum). Equation (2) can be rearranged in the form

$$\frac{1}{b^2} - \frac{f}{r^2} = \frac{1}{r^4}\left(\frac{\mathrm{d}r}{\mathrm{d}\phi}\right)^2 \geq 0. \tag{3}$$

The second term on the left-hand side

$$V(r) = \frac{f(r)}{r^2} \tag{4}$$

plays a role of an effective potential—a photon with an impact parameter b can propagate only in the regions where $1/b^2 \geq V(r)$. The turning points correspond to $1/b^2 = V$; hence, the radial location of the maximum of the effective photon potential corresponds to the unstable photon orbit and the value of b at the potential maximum is the radius of the observed photon ring. The effective photon potential is thus a useful tool to diagnose the black hole shadow. The shape of the effective photon potential is also relevant in the context of gravitational wave ringdowns, as discussed, for example, by Cardoso *et al.* [39], who explored a symmetric Schwarzschild wormhole case, and more recently by Horák *et al.* (in prep) [40], who discussed ultracompact stars.

Figure 1 shows the effective potential of a wormhole connecting two manifolds $\mathcal{R}_1$ and $\mathcal{R}_2$ at a throat located at $r = r_0$. Here $\mathcal{R}_1$ is a Schwarzschild spacetime. We denote $\xi = M_2/M_1$. For $\xi = 1$, we find a thin-shell symmetric wormhole of Visser [3]. The critical curve is formed by photons approaching the effective potential maximum. As long as the potential barrier is the same on both sides of the throat, the shape of the critical curve will be consistent with that corresponding to a black hole of mass M_1. However, if we construct a wormhole with an asymmetric effective potential, such as the blue curve $\xi = 1.5$ in Fig. 1, the situation will change dramatically. The observers in $\mathcal{R}_2$ should see a shadow associated with the effective potential maximum in $\mathcal{R}_2$, consistent with the expectations for the M_2 black hole, and formed by photons of impact parameter $\approx b_2$. However, they will also see a shadow feature associated with the photon effective potential maximum in $\mathcal{R}_1$, formed by photons with an impact parameter $\approx b_1$, of an unexpected diameter inconsistent with the expectations for the M_2 mass black hole. In Sec. IV, we show that such asymmetric effective potentials can be constructed by considering wormholes connecting Reissner-Nordström spacetimes.

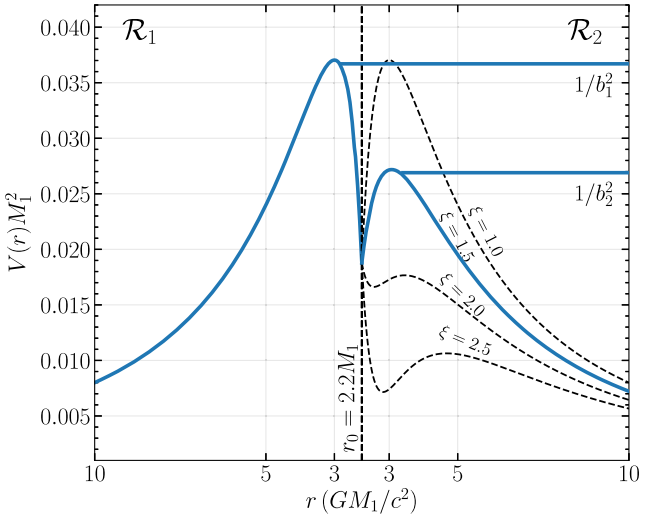

FIG. 1. Effective photon potential $V(r)$ for the asymmetric wormhole, obtained by connecting two manifolds $\mathcal{R}_1$ and $\mathcal{R}_2$. $\mathcal{R}_1$ is a fixed Schwarzschild spacetime, while $\mathcal{R}_2$ is a Reissner-Nordström spacetime matched for several values of an asymmetry parameter $\xi = M_2/M_1$. As an example, for $\xi = 1.5$, two photons with impact parameters b_1 and b_2 are shown. The photon with impact parameter b_2 is reflected at the effective-potential barrier as in ordinary Reissner-Nordström spacetime before it reaches the throat at r_0. On the other hand, the photon corresponding to b_1 crosses the potential barrier in $\mathcal{R}_2$, falls into the wormhole, but then it is reflected back to $\mathcal{R}_2$ by the $\mathcal{R}_1$ potential barrier.

III. REISSNER-NORDSTRÖM SPACETIME

In the case of the Reissner-Nordström spacetime, the function $f(r)$ in Eq. (1) is given by

$$f(r) = 1 - \frac{2M}{r} + \frac{\mathcal{Q}^2}{r^2}, \tag{5}$$

where M and $\mathcal{Q}$ are the mass and the electric charge parameters, respectively. For $\mathcal{Q}^2 \leq M^2$, the condition $f = 0$ implies the presence of two horizons, located at

$$r_{\mathrm{h}\pm} = M \pm (M^2 - \mathcal{Q}^2)^{1/2}, \tag{6}$$

and the metric describes a charged nonrotating black hole. We refer to the larger one, $r_{\mathrm{h}+}$, as an event horizon, while $r_{\mathrm{h}-}$ is a Cauchy horizon. We will denote the event horizon radius with r_{h}, that is, $r_{\mathrm{h}} \equiv r_{\mathrm{h}+}$. For $\mathcal{Q}^2 > M^2$, Reissner-Nordström metric describes a spherically symmetric charged naked singularity. The photon sphere (location of the spherical null geodesics) radius r_γ follows from the condition $\mathrm{d}V/\mathrm{d}r = 0$, which leads to the quadratic equation

$$r_\gamma^2 - 3Mr_\gamma + 2\mathcal{Q}^2 = 0 \tag{7}$$

with two roots

$$r_{\gamma\pm} = \frac{3M \pm (9M^2 - 8\mathcal{Q}^2)^{1/2}}{2}. \tag{8}$$

The larger solution $r_{\gamma+}$ corresponds to a local maximum of $V(r)$, related to the unstable photon orbit. Note also that the solutions $r_{\gamma\pm}$ exist only for $\mathcal{Q}^2 \leq \frac{9}{8}M^2$. We will denote the larger root with r_γ, that is, $r_\gamma \equiv r_{\gamma+}$.

The radius of the critical curve (shadow seen by a distant observer) is given by the critical impact parameter b_{c}, corresponding to the maximum of the effective potential,

$$b_{\mathrm{c}} = V_{\mathrm{max}}^{-1/2} = r_\gamma [f(r_\gamma)]^{-1/2}. \tag{9}$$

The location of the horizons $r_{\mathrm{h}\pm}$, photon spheres $r_{\gamma\pm}$, and the value of the critical impact parameter b_{c} as functions of $\mathcal{Q}^2/M^2$ are shown in Fig. 2. All the relevant radii r_{h}, r_γ, b_{c} decrease monotonically with $\mathcal{Q}^2$ [41]. Impact parameter decreases by ∼30% between $\mathcal{Q}^2/M^2 = 0$ and $\mathcal{Q}^2/M^2 = 9/8$. In certain alternative theories of gravity [42], negative $\mathcal{Q}^2$, reinterpreted as a gravitational "tidal charge," is admitted and yields larger b_{c}. However, we limit our discussion to $0 \leq \mathcal{Q}^2 \leq 9/8M^2$.

In a realistic astrophysical context, it is unlikely that a black hole could maintain an electric charge yielding $\mathcal{Q}^2$ comparable to M^2 [43]. However, it remains very unclear, what would constitute a realistic astrophysical context for an exotic object such as a traversable wormhole. Regardless of these concerns, Reissner-Nordström spacetime and Reissner-Nordström wormholes constitute a very useful simple model

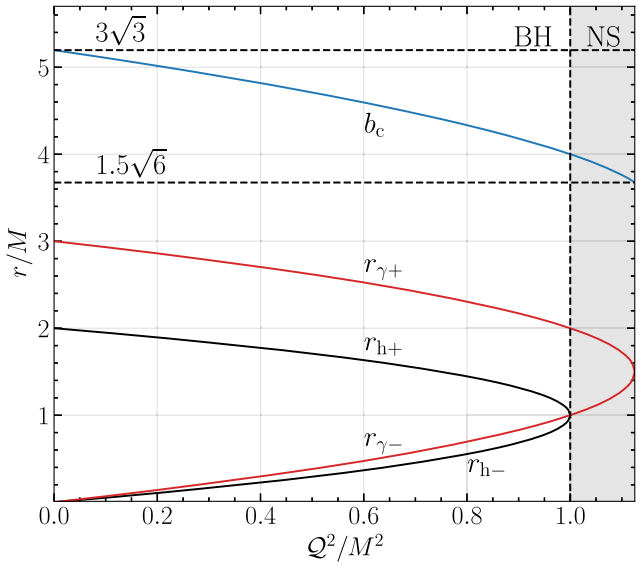

FIG. 2. Relevant radii in the Reissner-Nordström spacetime: event horizons $r_{\mathrm{h}\pm}$, photon spheres $r_{\gamma\pm}$, and the critical impact parameter b_{c}. For $\mathcal{Q}^2 \leq M^2$, the spacetime corresponds to a charged black hole. The shaded region for $1 < \mathcal{Q}^2 \leq 9/8M^2$ corresponds to a naked singularity solution.

to explore the deviations from the Schwarzschild case when $\sim r^{-2}$ term in $f(r)$ is introduced.

IV. MATCHING REISSNER-NORDSTRÖM SPACETIMES

It has been first noticed by Visser [3] that a traversable wormhole can be formed using a simple cut-and-paste technique applied to two Schwarzschild spacetimes. The necessary condition of matching the induced metrics at the junction is trivially fulfilled when Schwarzschild spacetimes corresponding to identical masses are matched at the same Boyer-Lidquist coordinate radius. The resulting wormhole is therefore reflection symmetric around the throat and so is the effective photon potential, as discussed in Sec. II. Reflection-asymmetric wormhole solutions formed by stitching two Schwarzschild and Reissner-Nordström spacetimes were presented by Garcia *et al.* [34]. Here we consider a simple cut-and-paste construction of an asymmetric Reissner-Nordström wormhole, where spacetime is static, location of the throat is constant in time, and we can explicitly match the full metric on both sides in Boyer-Lindquist coordinates. Because of the g_{tt} continuity, not demanded by a more general construction of reflection-asymmetric wormholes, we conserve the energy $E = -p_t$ of a photon crossing the wormhole throat.

To outline such a solution, let us consider two manifolds $\mathcal{R}_1$ and $\mathcal{R}_2$ arising from two different Reissner-Nordström spacetimes by cutting-off their interior parts at radii r_1 and r_2 (respectively), $\mathcal{R}_1 = \{r > r_1 | r_1 > r_{\rm h,1}\}$, $\mathcal{R}_2 = \{r > r_2 | r_2 > r_{\rm h,2}\}$, The two manifolds are then glued together by identifying their boundaries, $\partial\mathcal{R}_1 \equiv \partial\mathcal{R}_2 \equiv \Sigma$, Fig. 3. We require the metric coefficients $g_{\mu\nu}$ to remain continuous across the junction, that is, $g_{\mu\nu,1}|_\Sigma = g_{\mu\nu,2}|_\Sigma$. Derivatives of the metric may be discontinuous, reflecting the presence of a massive and charged thin shell that is the source of gravitational and electromagnetic field (e.g., [37]).

The conditions we impose at the junction are

$$r_1^2 = r_2^2 \equiv r_0^2, \tag{10}$$

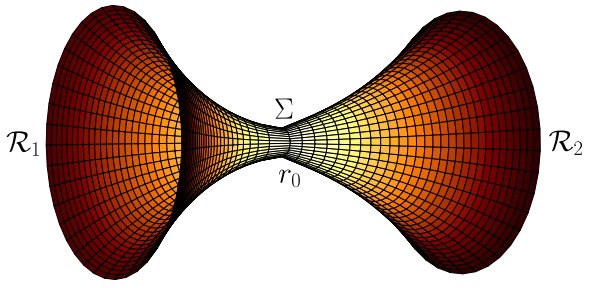

FIG. 3. Embedding diagram for a reflection-asymmetric thin-shell traversable wormhole with parameters $M_2 = 1.6M_1$, $r_0 = 2.1M_1$, $\mathcal{Q}_1^2 = 0$, $\mathcal{Q}_2^2 = 0.98M_2^2$.

$$f_1(r_0; M_1, \mathcal{Q}_1) = f_2(r_0; M_2, \mathcal{Q}_2), \tag{11}$$

where

$$f_{1,2}(r; M_{1,2}, \mathcal{Q}_{1,2}) = 1 - \frac{2M_{1,2}}{r} + \frac{\mathcal{Q}_{1,2}^2}{r^2}. \tag{12}$$

Condition (10) assures continuity of $g_{\phi\phi}$ and $g_{\theta\theta}$ components, while the later one (11) is required by the continuity of g_{tt} and g_{rr}. Note that under these assumptions matching Schwarzschild spacetimes with $M_1 \neq M_2$ is not possible, as $f_1(r_0, M_1, 0) = f_2(r_0, M_2, 0)$ implies $M_1 = M_2$. Introducing the asymmetry parameter

$$\xi = M_2/M_1, \tag{13}$$

we can now consider r_0, M_1, ξ, and $\mathcal{Q}_1$ to be fixed model parameters and use Eq. (11) to solve for the charge parameter $\mathcal{Q}_2^2$,

$$\mathcal{Q}_2^2 = 2r_0M_1(\xi - 1) + \mathcal{Q}_1^2. \tag{14}$$

Hence, we can fulfill conditions (10) and (11) for $M_1 \neq M_2$ if we consider Reissner-Nordström wormholes. Our construction constitutes a subset of the solutions considered by Garcia *et al.* [34] and Forghani *et al.* [35], who also studied their stability and related properties of the exotic matter concentrated at the throat. Instead, in the current paper, we are interested in the appearance of the reflection-asymmetric wormholes to a distant observer.

V. WORMHOLE APPEARANCE

We investigate in detail the parameter space in case of $\mathcal{Q}_1^2 \equiv 0$, so when $\mathcal{R}_1$ is a subset of a Schwarzschild spacetime. In Fig. 4, we see that this slice of the full parameter space is already very rich in terms of the wormhole shadow topologies. Depending on a combination of $\xi = M_2/M_1$ and r_0/M_1, manifold $\mathcal{R}_2$ can be a subset of a charged black hole (shaded gray) or a naked singularity (shaded red) spacetime. We first classify the wormhole solutions in terms of the presence of the photon orbit in $\mathcal{R}_{1,2}$, so whether $r_0 < r_\gamma$. As a result, possible cases indicated in Fig. 4 are as follows:

(1) Regions I and IV: $r_0 > r_{\gamma,1}$ and $r_0 > r_{\gamma,2}$, no photon sphere neither in $\mathcal{R}_1$ nor in $\mathcal{R}_2$
(2) Regions II and V: $r_0 < r_{\gamma,1}$ and $r_0 > r_{\gamma,2}$, photon sphere only in $\mathcal{R}_1$
(3) Regions III and VII: $r_0 < r_{\gamma,1}$ and $r_0 < r_{\gamma,2}$, photon spheres in both $\mathcal{R}_1$ and $\mathcal{R}_2$
(4) Region VI: $r_0 > r_{\gamma,1}$ and $r_0 < r_{\gamma,2}$, photon sphere only in $\mathcal{R}_2$

The presence of an unstable photon orbit on the opposite side of the wormhole is not a sufficient condition for a distant observer to see the corresponding critical curve—the photons still need to cross the effective photon potential

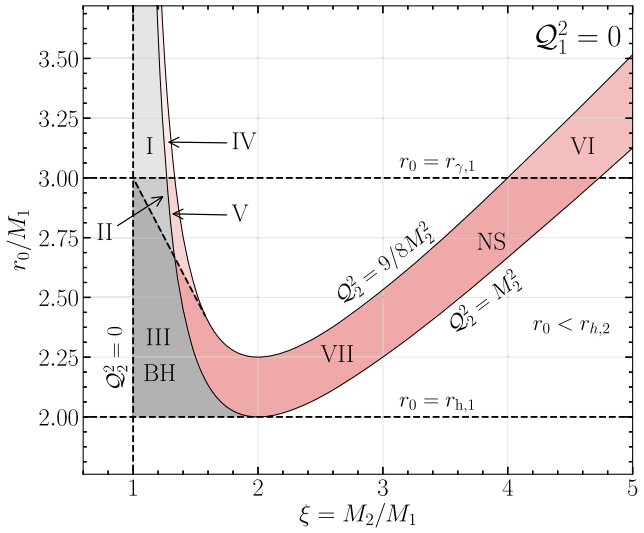

FIG. 4. Parameter space for $\mathcal{Q}_1 = 0$ with varying r_0/M_1 and ξ. $\mathcal{R}_2$ can be a subset of a Reissner-Nordström charged black hole spacetime (gray-shaded regions I–III) or a subset of a Reissner-Nordström naked singularity spacetime (red-shaded regions IV–VII). Roman numerals denote the presence of the photon sphere in $\mathcal{R}_{1,2}$ or lack thereof; see the text.

barrier on the observer's side. As an example, in Fig. 1, a distant observer in $\mathcal{R}_2$ sees critical curves associated with effective potential maxima in both $\mathcal{R}_1$ and $\mathcal{R}_2$, but the observer in $\mathcal{R}_1$ only sees critical curve associated with the effective potential maximum in $\mathcal{R}_1$. A simple condition for the observer in $\mathcal{R}_i$ to observe the critical curve from the other side of the wormhole is therefore given by

$$\max_{\mathcal{R}_i} V(r) < V(r_{\gamma,j}) \quad \text{and} \quad r_0 < r_{\gamma,j} \tag{15}$$

for $i \neq j$. Because we assume $\mathcal{Q}^2 \geq 0$, it follows from Eq. (14) that if $\mathcal{Q}_1 = 0$ then $\xi \geq 1$. In other words, we cannot match Schwarzshild spacetime with mass M_1 with a Reissner-Nordström spacetime of lower mass M_2 within the framework described in Sec. IV. Evaluating numerically condition (15) for the parameter space shown in Fig. 4, we find that under our assumptions the observer in $\mathcal{R}_1$ is never able to see the critical curve related to the photon sphere in $\mathcal{R}_2$. Hence, such an observer may only see the Schwarzschild spacetime critical curve, just as if the observed compact object was a nonrotating black hole. On the other hand, an observer in $\mathcal{R}_2$ can see the critical curve from $\mathcal{R}_1$ in all cases, as long as $r_0 < r_{\gamma,1} = 3M_1$.

The maximum of the effective potential occurs also for spacetime parameters from region I, at the throat of the wormhole. One may argue, that the throat at $r = r_0$ may also correspond to an unstable photon orbit, as it is in the case considered by Shaikh *et al.* [16]. However, in the vicinity of the throat, the radial derivative of the effective potential remains finite, having discontinuity across the throat. As a result, the null geodesics do not wind up around $r = r_0$ as in the case of an ordinary unstable photon orbit, where the radial derivatives approach zero. Rather, they are suddenly "reflected" to the other spacetime, creating a discontinuity in the observed image.

In Fig. 5, we evaluate the ratio between the size of the shadow originating in $\mathcal{R}_1$ observed from $\mathcal{R}_2$ and the expected shadow in $\mathcal{R}_2$, that is, $b_{\mathrm{c},1}/b_{\mathrm{c},2}$. What this means is that even if $r_0 > r_{\gamma,2}$, we use $b_{\mathrm{c},2}$ computed with Eq. (9), since a distant observer would not know about the throat location r_0 and would reasonably expect to see the shadow of a Reissner-Nordström object. The shadow seen through the wormhole may be as much as 3 times smaller than the expected one. In regions III and VII, these two shadows would appear simultaneously. Two such examples are shown in Fig. 6. In regions II and V, the $\mathcal{R}_2$ observer would only see the $\mathcal{R}_1$ shadow as $r_0 > r_{\gamma,2}$; nevertheless, for the considered wormhole model, its size would be quite close to the Reissner-Nordström $\mathcal{R}_2$ expectations. In region VI, only the ordinary shadow of $\mathcal{R}_2$ would be seen.

We find trajectories of photons in wormhole spacetimes constructed in Sec. IV by numerically integrating the null geodesic equations of motion. At the junction r_0, we use the fact that the metric is continuous and p_t and p_ϕ are conserved, while p_θ remains 0, as we consider an equatorial motion in a spherically symmetric spacetime. Then p_r only requires the sign reversal from ingoing to outgoing. Examples of photon trajectories are shown in Fig. 6.

In the first row of Fig. 6, a spacetime from region III of the parameter space, shown in Fig. 4, is considered. The embedding diagram for this particular wormhole was shown in Fig. 3. We are particularly interested in

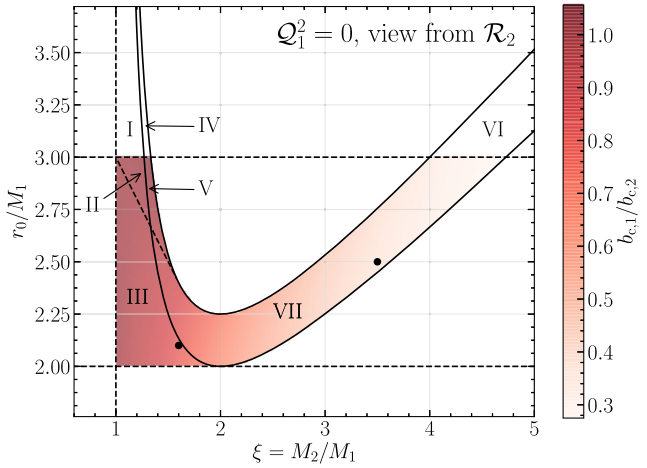

FIG. 5. The shaded region corresponds to the part of the parameter space, for which a distant observer in $\mathcal{R}_2$ sees a shadow associated with the photon sphere in $\mathcal{R}_1$ through the wormhole. The color codes ratio of the $\mathcal{R}_1$ shadow radius $b_{\mathrm{c},1}$ with respect to $b_{\mathrm{c},2}$, the expected radius of a Reissner-Nordström shadow of $\mathcal{R}_2$. Two black dots indicate parameters of the examples considered in Fig. 6.

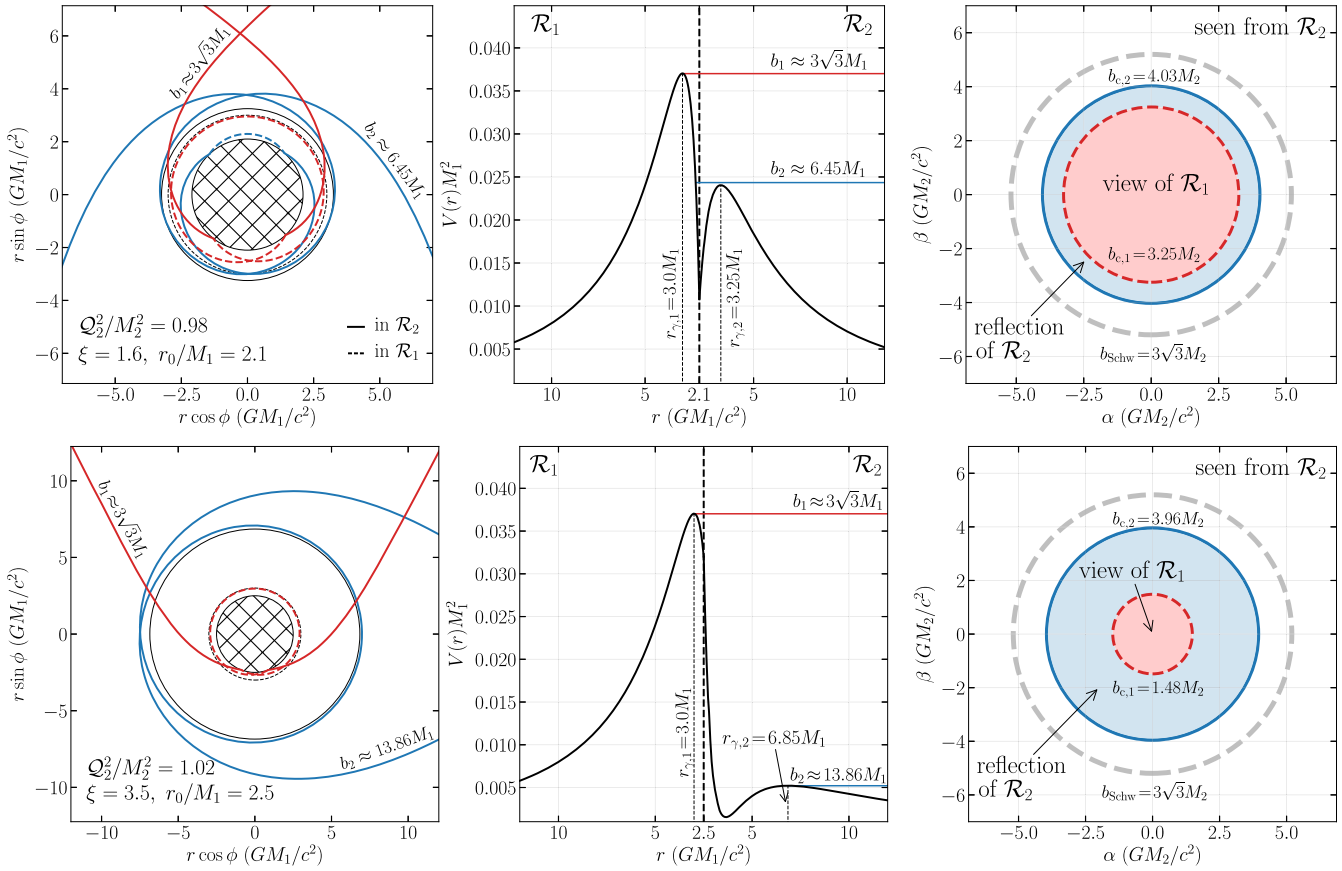

FIG. 6. Top row: properties of a wormhole connecting a Schwarzschild spacetime $\mathcal{R}_1$ with mass M_1 and a Reissner-Nordström spacetime $\mathcal{R}_2$ with mass $1.6M_1$ and charge $\mathcal{Q}_2^2 = 0.98M_2^2$. Left: trajectories of photons with the impact parameters close to critical values for $\mathcal{R}_1$ and $\mathcal{R}_2$. The hatched region corresponds to $r < r_0$ and is not a part of the investigated spacetime. Dashed lines indicate trajectories on the other side of the wormhole, that is in $\mathcal{R}_1$. Middle: the corresponding reflection-asymmetric effective photon potential. Locations of the unstable photon spheres (maxima of the effective potentials) are indicated. Right: an appearance of the wormhole for a distant observer. Two rings, corresponding to critical curves in $\mathcal{R}_1$ ($b_{c,1}$) and in $\mathcal{R}_2$ ($b_{c,2}$), are visible. A region in which photons visit $\mathcal{R}_1$ and are reflected back to $\mathcal{R}_2$ is shaded in blue. Celestial coordinates (α, β) are measured in GM_2/c^2. Bottom row: same, but for the $\mathcal{R}_2$ spacetime parameters $M_2 = 3.5M_1$ and $\mathcal{Q}_2^2 = 1.02M_2^2$.

trajectories approaching the unstable photon sphere on each side of the wormhole. Trajectory b_1 corresponds to a photon emitted in $\mathcal{R}_2$ with an impact parameter slightly larger (so $1/b_1^2$ slightly smaller) than the critical value in $\mathcal{R}_1$ of $b_{c,1} = 3\sqrt{3}M_1$. The photon falls into a wormhole from $\mathcal{R}_2$ and crosses the throat. It then loops around the unstable photon sphere in $\mathcal{R}_1$ (top left panel) but ultimately is reflected back into the $\mathcal{R}_2$ by the $\mathcal{R}_1$ effective potential barrier (top middle panel). Photon b_2 corresponds to the impact parameter slightly smaller than the critical value in $\mathcal{R}_2$ (or $1/b_2^2$ slightly larger). Therefore, it loops around the photon sphere in $\mathcal{R}_2$ (top left panel), but ultimately falls into the wormhole, only to be quickly reflected back to $\mathcal{R}_2$ by the $\mathcal{R}_1$ potential barrier (top middle panel). The top right panel of Fig. 6 outlines the appearance of the wormhole shadow seen by a distant observer. The dashed gray line shows the Schwarzschild critical curve for the mass M_2. The continuous blue line $b_{c,2}$ is the critical curve for the $\mathcal{R}_2$ Reissner-Nordström spacetime with mass M_2 and charge parameter $\mathcal{Q}_2^2 = 0.98M_2^2$ [from Eq. (14)]. The dashed red line is the critical curve from $\mathcal{R}_1$, seen through the wormhole, corresponding to that of a Schwarzschild black hole of mass M_1, with radius $b_{c,1}$. Inside this circle there is a region where a view of the $\mathcal{R}_1$ spacetime is seen through the wormhole (shaded red). Between the two shadow features, a reflection of the $\mathcal{R}_2$ (shaded blue), formed by the photons that visited $\mathcal{R}_1$ but were reflected back into $\mathcal{R}_2$ by the potential barrier, is seen. A similar scenario, but with a wormhole spacetime from region V of the parameter space, is investigated in Fig. 6, bottom row. In this case, the two photon rings are of a very different size, $b_{c,1}/b_{c,2} = 0.37$.

VI. DISCUSSION

We have presented results characterizing the impact of reflection asymmetry of the effective photon potential on the appearance of a wormhole to a distant observer. As an instructive example we considered a family of thin-shell,

traversable, reflection-asymmetric wormholes, obtained by surgically grafting two Reissner-Nordström spacetimes with a cut-and-paste procedure [3,34].

We notice interesting features in the shadow (critical curve related to photon geodesics approaching the unstable photon sphere, as systematically defined and discussed by, e.g., [28,29]) of a reflection-asymmetric wormhole. Apart from variation of the shadow diameter with respect to the expectations, for certain model parameters, observers on one side of the wormhole may be able to see both the shadow corresponding to the photon sphere on their side, and the shadow corresponding to the photon sphere from the other side of the wormhole. While several authors considered wormhole shadows before (e.g., Refs. [12–15]), a critical curve consisting of a double circle is a rather uncommon feature in the literature. Nevertheless, similar shadows were recently reported by Shaikh *et al.* [16], who considered reflection-symmetric traversable wormholes with a secondary maximum of the photon effective potential located at the throat. Wang *et al.* [36] discussed shadows of asymmetric Schwarzschild wormholes, for which photon energy $E = -p_t$ is not conserved when a photon crosses the throat.

Vincent *et al.* [32] presented ray-traced images of several types of black hole mimickers surrounded by an accretion disk, including a Lamy spinning wormhole [44]. In Fig. 10 and Fig. B.1 of [32], images similar to the ones described in this paper (i.e., the shadow appearing as multiple circular features) can be seen. The Lamy metric is identical to that of Kerr, with the only difference that the mass of the object M is replaced by a function of the radial coordinate $M(r)$. For large $|r|$, Lamy metric approaches Kerr. In either case, two effective photon potentials for the equatorial plane can be defined as

$$V_\pm \equiv V_\pm(r) = \frac{-g_{t\varphi} \pm \sqrt{g_{t\varphi}^2 - g_{tt} g_{\varphi\varphi}}}{g_{\varphi\varphi}}. \tag{16}$$

In Fig. 7, we show the $V_\pm(r)$ functions for the parameter values considered in [32]. The motion of photons in the equatorial plane is restricted to the region above V_+ or below V_-. The asymmetry of the Lamy potentials $V_\pm(r)$ with respect to $r = 0$ leads to multiple critical curves on sky. We however note that this analysis is only valid in the equatorial plane and that equatorial geodesics only matter for an exactly edge-on view. A more detailed treatment is necessary in order to fully understand the non-edge-on images, such as those presented in [32]. Nevertheless, we can conclude that the Lamy wormhole is another example of a reflection-asymmetric wormhole spacetime, indicating multiple critical curves.

Several authors discussed observational constraints on existence of wormholes derived from variety of phenomena [45–50]. Observing geometry of the shadows of compact objects is a particularly promising avenue. Features such as the presence of multiple critical curves, topologically different from the "classic" Kerr black hole shadow [30,31], could potentially constitute a much more powerful discriminant of black hole mimickers than a moderate difference in the critical curve size and circularity. This is particularly important in view of significant uncertainties related to distance and mass of sources that could be potentially resolved by future extremely long baseline radio interferometry observations [22], perhaps with a single exception of our Galactic Center. However, while detection of multiple bright rings on sky would indicate that the observed compact object is not a Kerr black hole, it would not necessarily imply the nonexistence of an event horizon. A counterexample is given by the black holes with scalar hair, as studied by [51–53].

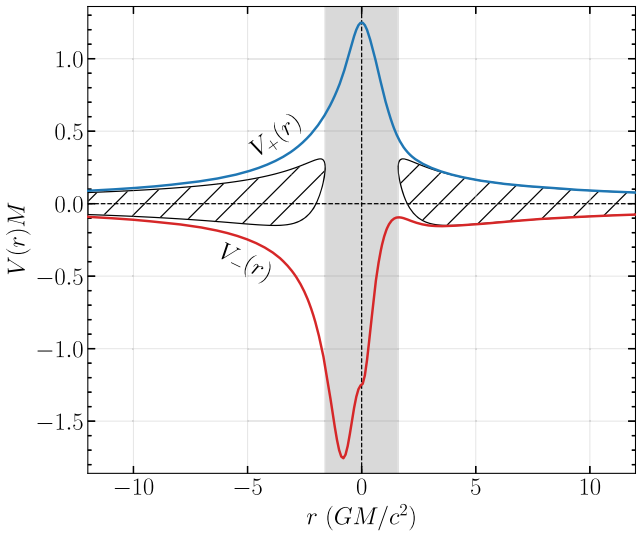

FIG. 7. Asymmetric equatorial effective photon potential of a Lamy wormhole for the parameters considered by [32]: dimensionless spin $a_* = 0.8$, charge $b = M$. There are two extrema of the effective potential V_- associated with unstable spherical photon orbits and affecting retrograde photons, one at about $3.5M$ and other at about $-0.8M$. Potential V_+ has a single maximum at $0M$. For comparison, the hatched region represents the forbidden region between V_- and V_+ for a Kerr spacetime. The shaded region indicates the interior of the Kerr event horizon, $|r| < 1.6M$.

Another property of a traversable wormhole image is the presence of a central region directly illuminated by the low angular momentum photons from the other side of the wormhole. Detecting such a feature would also potentially constitute a robust discriminant of some black hole mimickers [25].

Apart from these properties, images of reflection-asymmetric wormholes would contain a region in which photons emitted on one side of the wormhole visit the other side and are reflected back to the side of their origin (blue-shaded region in the right column of Fig. 6). If such

a region would ever be observed, its presence could potentially allow for probing the geometry on the other side of a wormhole through investigating delays between the directly observed and reflected events. Such a special region is exclusively present in the images of the reflection-asymmetric wormholes. Fundamentally, it is not even necessary to resolve the source in order to investigate this property—it could manifest as a delayed correlated component in the compact object's light curve. Search for such a feature could already be performed with the existing light curve databases.

ACKNOWLEDGMENTS

We thank Danial Forghani, Eric Gourgoulhon, Otakar Svítek, Tayebeh Tahamtan, and Ronaldo Vieira for useful comments. M. W. wishes to thank the Astronomical Institute in Prague for hospitality. This work was supported in part by the INTER-EXCELLENCE Project No. LTI17018 aimed to strengthen international collaboration of Czech scientific institutions, and the Black Hole Initiative at Harvard University, which is funded by grants from the John Templeton Foundation and the Gordon and Betty Moore Foundation to Harvard University.

[1] H. G. Ellis, Ether flow through a drainhole: A particle model in general relativity, J. Math. Phys. (N.Y.) **14**, 104 (1973).
[2] M. S. Morris, K. S. Thorne, and U. Yurtsever, Wormholes, Time Machines, and the Weak Energy Condition, Phys. Rev. Lett. **61**, 1446 (1988).
[3] M. Visser, Traversable wormholes from surgically modified Schwarzschild spacetimes, Nucl. Phys. **B328**, 203 (1989).
[4] E. Poisson and M. Visser, Thin-shell wormholes: Linearization stability, Phys. Rev. D **52**, 7318 (1995).
[5] E. Gravanis and S. Willison, "Mass without mass" from thin shells in Gauss-Bonnet gravity, Phys. Rev. D **75**, 084025 (2007).
[6] T. Harko, F. S. N. Lobo, M. K. Mak, and S. V. Sushkov, Modified-gravity wormholes without exotic matter, Phys. Rev. D **87**, 067504 (2013).
[7] P. H. R. S. Moraes and P. K. Sahoo, Nonexotic matter wormholes in a trace of the energy-momentum tensor squared gravity, Phys. Rev. D **97**, 024007 (2018).
[8] O. Svítek and T. Tahamtan, Nonsymmetric dynamical thin-shell wormhole in Robinson-Trautman class, Eur. Phys. J. C **78**, 167 (2018).
[9] K. K. Nandi, Y.-Z. Zhang, and A. V. Zakharov, Gravitational lensing by wormholes, Phys. Rev. D **74**, 024020 (2006).
[10] N. Tsukamoto, T. Harada, and K. Yajima, Can we distinguish between black holes and wormholes by their Einstein-ring systems?, Phys. Rev. D **86**, 104062 (2012).
[11] C. Bambi, Can the supermassive objects at the centers of galaxies be traversable wormholes? The first test of strong gravity for mm/sub-mm very long baseline interferometry facilities, Phys. Rev. D **87**, 107501 (2013).
[12] P. G. Nedkova, V. K. Tinchev, and S. S. Yazadjiev, Shadow of a rotating traversable wormhole, Phys. Rev. D **88**, 124019 (2013).
[13] T. Ohgami and N. Sakai, Wormhole shadows, Phys. Rev. D **91**, 124020 (2015).
[14] A. Abdujabbarov, B. Juraev, B. Ahmedov, and Z. Stuchlík, Shadow of rotating wormhole in plasma environment, Astrophys. Space Sci. **361**, 226 (2016).
[15] R. Shaikh, Shadows of rotating wormholes, Phys. Rev. D **98**, 024044 (2018).
[16] R. Shaikh, P. Banerjee, S. Paul, and T. Sarkar, A novel gravitational lensing feature by wormholes, Phys. Lett. B **789**, 270 (2019).
[17] M. Amir, K. Jusufi, A. Banerjee, and S. Hansraj, Shadow images of Kerr-like wormholes, Classical Quantum Gravity **36**, 215007 (2019).
[18] S. S. Doeleman, J. Weintroub, A. E. E. Rogers, R. Plambeck, R. Freund, R. P. J. Tilanus, P. Friberg, L. M. Ziurys, J. M. Moran, B. Corey, K. H. Young, D. L. Smythe, M. Titus, D. P. Marrone, R. J. Cappallo, D. C. J. Bock, G. C. Bower *et al.*, Event-horizon-scale structure in the supermassive black hole candidate at the Galactic Centre, Nature (London) **455**, 78 (2008).
[19] S. S. Doeleman, V. L. Fish, D. E. Schenck, C. Beaudoin, R. Blundell, G. C. Bower, A. E. Broderick, R. Chamberlin, R. Freund, P. Friberg, M. A. Gurwell, P. T. P. Ho, M. Honma, M. Inoue, T. P. Krichbaum *et al.*, Jet-launching structure resolved near the supermassive black hole in M87, Science **338**, 355 (2012).
[20] Event Horizon Telescope Collaboration *et al.*, First M87 Event Horizon Telescope Results. I. The shadow of the supermassive black hole, Astrophys. J. Lett. **875**, L1 (2019).
[21] M. Wielgus, K. Akiyama, L. Blackburn, C.-K. Chan, J. Dexter, S. S. Doeleman, V. L. Fish, S. Issaoun, M. D. Johnson, T. P. Krichbaum, R.-S. Lu, D. W. Pesce, G. N. Wong, G. C. Bower, A. E. Broderick *et al.*, Monitoring the morphology of M87* in 2009-2017 with the EHT, Astrophys. J. **901**, 67 (2020).
[22] M. Johnson, K. Haworth, D. W. Pesce, D. C. M. Palumbo, L. Blackburn, K. Akiyama, D. Boroson, K. L. Bouman, J. R. Farah, V. L. Fish, M. Honma, T. Kawashima, M. Kino, A. Raymond, M. Silver *et al.*, Studying black holes on horizon scales with space-VLBI, arXiv:1909.01405.
[23] D. Pesce, K. Haworth, G. J. Melnick, L. Blackburn, M. Wielgus, M. D. Johnson, A. Raymond, J. Weintroub, D. C. M. Palumbo, S. S. Doeleman, and D. J. James, Extremely long baseline interferometry with Origins Space Telescope, arXiv:1909.01408.
[24] D. Psaltis, Testing general relativity with the Event Horizon Telescope, Gen. Relativ. Gravit. **51**, 137 (2019).

[25] Event Horizon Telescope Collaboration *et al.*, First M87 Event Horizon Telescope Results. V. Physical origin of the asymmetric ring, Astrophys. J. Lett. **875**, L5 (2019).
[26] C.-M. Claudel, K. S. Virbhadra, and G. F. R. Ellis, The geometry of photon surfaces, J. Math. Phys. (N.Y.) **42**, 818 (2001).
[27] E. Teo, Spherical photon orbits around a Kerr black hole, Gen. Relativ. Gravit. **35**, 1909 (2003).
[28] S. E. Gralla, D. E. Holz, and R. M. Wald, Black hole shadows, photon rings, and lensing rings, Phys. Rev. D **100**, 024018 (2019).
[29] M. D. Johnson, A. Lupsasca, A. Strominger, G. N. Wong, S. Hadar, D. Kapec, R. Narayan, A. Chael, C. F. Gammie, P. Galison, D. C. M. Palumbo, S. S. Doeleman, L. Blackburn, M. Wielgus, D. W. Pesce *et al.*, Universal interferometric signatures of a black hole's photon ring, Sci. Adv. **6**, eaaz1310 (2020).
[30] J. M. Bardeen, Timelike and null geodesics in the Kerr metric, in *Black Holes (Les Astres Occlus)*, edited by C. Dewitt and B. S. Dewitt (1973), pp. 215–239.
[31] J.-P. Luminet, Image of a spherical black hole with thin accretion disk, Astron. Astrophys. **75**, 228 (1979), http://articles.adsabs.harvard.edu/pdf/1979A%26A....75..228L.
[32] F. H. Vincent, M. Wielgus, M. A. Abramowicz, E. Gourgoulhon, J. P. Lasota, T. Paumard, and G. Perrin, Geometric modeling of M87* as a Kerr black hole or a non-Kerr compact object, arXiv:2002.09226.
[33] P. Schneider, J. Ehlers, and E. E. Falco, *Gravitational Lenses* (Springer, 1992).
[34] N. M. Garcia, F. S. N. Lobo, and M. Visser, Generic spherically symmetric dynamic thin-shell traversable wormholes in standard general relativity, Phys. Rev. D **86**, 044026 (2012).
[35] S. Forghani, S. Mazharimousavi, and M. Halilsoy, Asymmetric thin-shell wormholes, Eur. Phys. J. C **78**, 10.1140/epjc/s10052-018-5776-2 (2018).
[36] X. Wang, P.-C. Li, C.-Y. Zhang, and M. Guo, A novel shadow from the thin-shell wormhole, arXiv:2007.03327.
[37] E. F. Eiroa and G. E. Romero, Linearized stability of charged thin-shell wormholes, Gen. Relativ. Gravit. **36**, 651 (2004).
[38] M. Sharif and M. Azam, Reissner-Nordström thin-shell wormholes with generalized cosmic Chaplygin gas, Eur. Phys. J. C **73**, 2554 (2013).
[39] V. Cardoso, E. Franzin, and P. Pani, Is the Gravitational-Wave Ringdown a Probe of the Event Horizon?, Phys. Rev. Lett. **116**, 171101 (2016).
[40] J. Horák, K. Klimovicová, and M. A. Abramowicz Ringdowns from ultracompact stars: analytical formulae for damping of the trapped gravitational waves (in preparation).
[41] A. F. Zakharov, Particle capture cross sections for a Reissner–Nordström black hole, Classical Quantum Gravity **11**, 1027 (1994).
[42] N. Dadhich, R. Maartens, P. Papadopoulos, and V. Rezania, Black holes on the brane, Phys. Lett. B **487**, 1 (2000).
[43] R. M. Wald, Black hole in a uniform magnetic field, Phys. Rev. D **10**, 1680 (1974).
[44] F. Lamy, E. Gourgoulhon, T. Paumard, and F. H. Vincent, Imaging a non-singular rotating black hole at the center of the Galaxy, Classical Quantum Gravity **35**, 115009 (2018).
[45] D. F. Torres, G. E. Romero, and L. A. Anchordoqui, Might some gamma ray bursts be an observable signature of natural wormholes?, Phys. Rev. D **58**, 123001 (1998).
[46] R. Takahashi and H. Asada, Observational upper bound on the cosmic abundances of negative-mass compact objects and Ellis wormholes from the sloan digital sky survey quasar lens search, Astrophys. J. Lett. **768**, L16 (2013).
[47] M. Zhou, A. Cardenas-Avendano, C. Bambi, B. Kleihaus, and J. Kunz, Search for astrophysical rotating Ellis wormholes with x-ray reflection spectroscopy, Phys. Rev. D **94**, 024036 (2016).
[48] D.-C. Dai and D. Stojkovic, Observing a wormhole, Phys. Rev. D **100**, 083513 (2019).
[49] V. De Falco, E. Battista, S. Capozziello, and M. De Laurentis, General relativistic Poynting-Robertson effect to diagnose wormholes existence: Static and spherically symmetric case, Phys. Rev. D **101**, 104037 (2020).
[50] J. H. Simonetti, M. J. Kavic, D. Minic, D. Stojkovic, and D.-C. Dai, A sensitive search for wormholes, arXiv:2007.12184.
[51] C. A. R. Herdeiro and E. Radu, Kerr Black Holes with Scalar Hair, Phys. Rev. Lett. **112**, 221101 (2014).
[52] P. V. P. Cunha, J. Grover, C. Herdeiro, E. Radu, H. Rúnarsson, and A. Wittig, Chaotic lensing around boson stars and Kerr black holes with scalar hair, Phys. Rev. D **94**, 104023 (2016).
[53] F. H. Vincent, E. Gourgoulhon, C. Herdeiro, and E. Radu, Astrophysical imaging of Kerr black holes with scalar hair, Phys. Rev. D **94**, 084045 (2016).